Journal of Materials Chemistry A

ROYAL SOCIETY OF CHEMISTRY

PAPER

View Article Online
View Journal | View Issue

Cite this: J. Mater. Chem. A, 2020, 8, 17725

Uniformizing the electric field distribution and ion migration during zinc plating/stripping *via* a binary polymer blend artificial interphase†

Zhengang Li, ‡[ac] Wenjun Deng,‡[a] Chang Li,[a] Weijian Wang,[a] Zhuqing Zhou,[a] Yibo Li,[a] Xinran Yuan,[a] Jun Hu,[a] Man Zhang,[a] Jinlin Zhu,[a] Wei Tang, *[c] Xin Wang *[b] and Rui Li *[a]

Received 23rd May 2020
Accepted 5th August 2020

DOI: 10.1039/d0ta05253a

rsc.li/materials-a

Aqueous zinc hybrid capacitors are receiving intensive scientific interest due to them having the merits of both capacitors and batteries in achieving safety, high power and energy density, as well as long cycle life. Nonetheless, the dendrite growth and side reactions at the Zn/electrolyte interface are the biggest obstacles preventing them from large-scale applications. Here, we show that a non-conductive polyacrylamide (PAM)/polyvinylpyrrolidone (PVP) binary blend layer coated on a Zn anode can effectively suppress Zn dendrites and side reactions. The precise combination of ultra-high molecular weight PAM and low molecular weight PVP provides an excellent artificial anode/electrolyte interfacial layer with balanced adhesion, mechanical strength and hydrophilicity. The binary polymer interphase fundamentally uniformizes the localized electric field to regulate the ion migration in Zn plating/stripping, giving rise to superior electrochemical performance for the aqueous zinc hybrid capacitors. This study represents a promising approach for mitigating the long-lasting Zn dendrite growth issue.

Introduction

Electrochemical energy storage systems with high energy and power densities are urgently needed for the storage of intermittent renewable energy sources, such as solar, wind and tidal energy.[1–3] Rechargeable nonaqueous lithium ion batteries (LIBs) have been widely used in electric vehicles and portable electronics; however, the low power density and short lifespan features are still limiting their large-scale application towards long-term durability and high-power density.[4,5] Electric double layer capacitors (EDLCs) with the merits of high power density ($\approx$10 kW kg^{-1}) and superior lifespans (up to 100 000 cycles) have been regarded as a promising energy storage device. In an EDLC, the energy is stored and released *via* physically adsorbed ions in a Helmholtz double layer at the electrode–electrolyte interphase at a rapid charge transfer rate. Nevertheless, the low energy density ($\approx$10 W h^{-1} kg^{-1}) has restricted their potential for large-scale application.[6,7] A hybrid supercapacitor can be constructed by combing a battery-type electrode with a capacitor-type electrode to achieve high energy density, superior power density and long cycle life.[7] However, further development towards large-scale applications of Li-ion based supercapacitors is still restricted by costly insufficient lithium sources and flammability, on top of the high cost of organic electrolytes.[8,9] Thus, exploring novel high energy-density hybrid supercapacitors without sacrificing their cycle life, especially using more cost-effective and environmentally-friendly aqueous electrolytes, is essential for the large-scale energy storage application of such devices.

Metallic Zn has been recognized as an alternative anode for hybrid supercapacitors owing to its high theoretical capacity (5855 mA h cm^{-3} or 823 mA h g^{-1}), low electrochemical potential (−0.76 V *vs.* standard hydrogen electrode) and low cost.[10–12] Recently, some studies of Zn ion hybrid supercapacitors have been reported.[13–17] For example, a Zn ion hybrid supercapacitor integrated with Zn foil and active carbon (AC) in 2 M $Zn(SO_4)_2$ electrolyte was developed that exhibits a 10 000 cycle life, benefiting from the good stability of the EDLC-type cathode. Moreover, the narrow operating voltage (typically 0.2–1.8 V) of aqueous $ZnSO_4$ electrolytes has limited the running of hybrid supercapacitors, which is owing to the competitive hydrogen evolution (<0.2 V *vs.* Zn^{2+}/Zn) and oxygen evolution (>1.8 V *vs.* Zn^{2+}/Zn) of water.[13] Using a nonaqueous solvent (*e.g.*, acetonitrile) and increasing the concentration of zinc salt (3 M Zn $(CF_3SO_3)_2$) can somewhat widen the operating voltage of Zn-based hybrid supercapacitors.[15] However, Zn

[a]School of Advanced Materials, Peking University Shenzhen Graduate School, Shenzhen, 518055, China. E-mail: liruisz@pku.edu.cn

[b]Academy for Advanced Interdisciplinary Studies, Southern University of Science and Technology, Shenzhen, 518055, China. E-mail: wangx@sustech.edu.cn

[c]School of Chemical Engineering and Technology, Xi'an Jiaotong University, Xi'an, 710049, China. E-mail: tangw2018@mail.xjtu.edu.cn

† Electronic supplementary information (ESI) available. See DOI: 10.1039/d0ta05253a

‡ These authors contributed equally to this work.

metal is thermodynamically unstable with poor electrochemical reversibility in aqueous environments due to the corrosion caused by dissolved O_2 and free water,[18] as well as the uncontrollable Zn dendrite growth and low stripping/plating efficiency that occur at the interface between the Zn electrode and aqueous electrolyte.[19,20] In order to address these issues, multiple approaches have been explored. A number of electrolytes have been proposed by decreasing the free water content to inhibit the artificial reaction, such as ion-conductive polymer electrolytes,[21] solid-state electrolytes,[22,23] ultrahigh concentration 1 M $Zn(TFSI)_2$ + 20 M LiTFSI electrolyte,[24] 30 M $ZnCl_2$,[25] $Zn(ClO_4)_2$,[26] and $Zn(CF_3SO_3)_2$,[27] "water-in-deep eutectic solvent" of urea electrolytes,[28] salt-concentrated acetate electrolytes,[29] and hydrogel electrolytes.[30] However, the high viscosity and low conductivity of ultra-concentrated electrolytes remains an issue that needs to be further addressed.[31] Some groups have proposed constructing an *in situ* or *ex situ* artificial layer to prevent direct contact between the Zn electrode and aqueous electrolyte as a means to further improve the zinc deposition quality and restrain zinc dendrite growth.[32] These techniques and materials, including epitaxial electrodeposition,[33] a nanoporous $CaCO_3$ layer,[34] a polyamide buffer layer,[35] nanosized MOFs,[36,37] and TiO_2 [38] and ZrO_2 coatings,[39] were found to be promisingly effective.

Herein, we report that a coating layer of an electrically insulting polymer blend, polyacrylamide/polyvinylpyrrolidone or PAM/PVP, can be used as an artificial interphase to guide the Zn ion distribution during the plating/stripping process, thus effectively suppressing the growth of Zn dendrites. PAM/PVP have polar groups (C=O and N–H bonds) that can offer abundant adsorption sites. This is beneficial in several ways: (a) guiding the migration of Zn^{2+} along the polymer chains to the reaction interface, leading to more uniform zinc deposition; (b) acting as an electrostatic shield layer to avoid accumulation of Zn^{2+}/electrons on the tips, thus suppressing the growth of zinc dendrites; and (c) widening the electrochemical window to inhibit the water/O_2 corrosion. Benefiting from the effective suppression of side reactions and zinc dendrite growth, the PAM/PVP-coated Zn symmetric cell exhibits a long cycle life over 2220 h at a current density of 0.2 mA cm^{-2}, and a high reversibility for Zn stripping/plating with an average coulombic efficiency (CE) of 98.8% at 1 mA cm^{-2} after 100 cycles. In addition, with the employment of a PAM/PVP layer, the PAM/PVP-coated Zn-activated carbon (AC) hybrid supercapacitor demonstrated a superior electrochemical performance, including an increased operating voltage up to 2.0 V, high discharge capacitance (336 F g^{-1} at 0.5 A g^{-1}), good rate capability (≈49.1% capacitance retention at 30 A g^{-1}), high energy/power density (118 W h^{-1} kg^{-1}/17.9 kW kg^{-1} based on the mass of AC materials), and excellent cycling stability with 100% capacitance retention of the initial specific capacitances after 6000 cycles at 15 A g^{-1}.

Results and discussion

The polymers employed in the study are PAM and PVP, with a weight-average molecular weight of over 2 000 000 and 10 000 g mol^{-1}, respectively. The chemical structures are shown in Fig. 1. The polymer interphase layer on Zn was prepared by solvent-casting from an aqueous solution. The complete dissolution of the binary polymer blend in H_2O ensures a fully dissolved state of the molecular chains, which is critical for the firm adhesion between the Zn substrate and the polymer during solvent-casting. The combination of ultra-high molecular weight PAM and low molecular weight PVP leads to an ideal balance between adhesion, mechanical force and hydrophilicity of the polymer blend in water, allowing the passing of ions through the layer, while maintaining the framework of the coating during charging and discharging. Both polymers are amorphous, with glass transition temperatures (T_g's) over 100 °C. A polymer film containing a stoichiometric amount of $Zn(CF_3SO_3)_2$ electrolyte as in the hybrid capacitor was used for the investigation of the thermal stability. As a comparison, a pristine polymer sample was also investigated, as shown in Fig. 1a. Both curves exhibit a 10–15% weight loss at around 100 °C because of the moisture absorbed by the hydrophilic sample. The degradation of both samples initiates above 300 °C. This temperature is way above the service temperature of hybrid capacitors, so the thermal stability of the device can be ensured. To further investigate the phase transition with temperature, DSC of the PAM/PVP polymer film containing about 16 wt% water was performed from 30 °C to 220 °C (Fig. 1b). The first heating run on the DSC thermogram shows a single T_g at about 69 °C, suggesting a homogeneous system of the polymer blend in water. The second and the third heating curves on the DSC thermogram of the polymer blend are essentially identical, confirming the reversibility of the thermal transitions. Since the sample was first heated to 200 °C, the water was completely removed in the second and the third run, leaving only the thermal behavior of the bulk polymer. The third heating run demonstrates a typical thermal behavior of a binary system with two T_g's at about 140 °C and 200 °C, corresponding to the respective glass transition of PVP and PAM.[40] As a comparison,

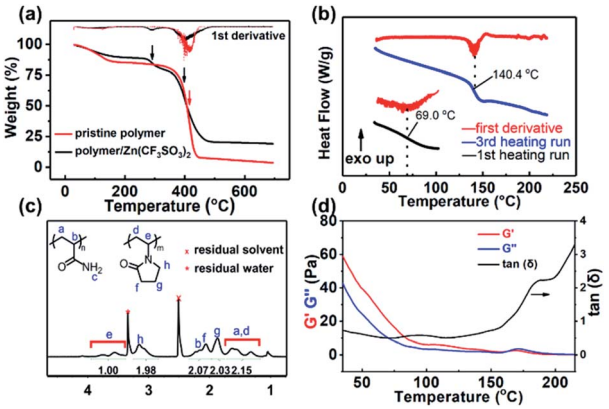

Fig. 1 Structures and properties of the PAM/PVP blend. (a) TGA thermogram of the pristine PAM/PVP and the PAM/PVP containing a stoichiometric amount of $Zn(CF_3SO_3)_2$ as in the hybrid capacitor. (b) 1st and 3rd DSC heating thermograms of the PAM/PVP blend. (c) ^1H NMR spectrum of PAM/PVP in DMSO-d_6 with the peak assignment and integrations shown on the graph. (d) Dynamic mechanical thermal analysis of a cast PAM/PVP film.

the thermal behavior of a polymer blend sample containing a stoichiometric amount of electrolyte as in the hybrid capacitor was also investigated and the results are shown in Fig. S1.† Similarly, the glass transition of PVP was found around 140 °C. The glass transition of PAM is hardly noticeable in both samples due to its small portion in the blend. However, the high molecular weight PAM, taking up less than 5 wt% of the blend (Fig. 1c), is critical in ensuring the strong adhesion of the polymer blend to the Zn anode. PAM with ultra-high molecular weight is super water absorbent and binds tightly to active surfaces *via* many polar amide groups. This provides constant adhesion of the polymer layer to the Zn anode during the whole charge–discharge cycles. PVP has a pendant five-membered ring structure that is very stable. Like PAM, PVP also has very polar groups that allows the migration of ions during charging and discharging.[41] Some recent research showed that PVP has structure-regulating properties that prevent the aggregation of nanoparticles *via* the steric effect.[42] The non-conductive yet polar character of the pyrrolidone groups makes PVP an excellent regulating layer for Zn anodes.[35] As shown in the dynamic mechanical thermal analysis of the PAM/PVP blend in Fig. 1d, the polymer blend shows a typical viscoelastic behavior with a glass transition from room temperature to about 85 °C. Similarly, for the gel form of the polymer blend, the fact that the storage modulus is higher than the loss modulus in a wide rotational range also demonstrates the viscoelastic behavior, as seen in Fig. S2.† The viscoelastic character is important in maintaining the strong adhesion of the polymer layer to the Zn substrate, as well as compensating the volume change during the charge–discharge cycles.

The electrochemical stability of the Zn anode was evaluated by analyzing the galvanostatic cycling performance of a symmetrical Zn cell. Nyquist plots of symmetrical Zn batteries reveal the influence of the PAM/PVP coating on the Zn^{2+} conductivity in the batteries (Fig. S3†). At a current density of 0.2 mA cm^{-2}, an irreversible and drastic rise of polarization voltage after cycling for 182 h (Fig. 2a) and an irregular voltage curve after 45 h of stripping/plating (Fig. 2b) are detected in the bare Zn symmetric cell. The cell failure originates from the by-product formation and competitive H_2 evolution reaction (HER), which was confirmed by the obvious battery volume expansion (Fig. S4†). On the contrary, the PAM/PVP-coated Zn anodes display a long stability over 2220 h with a very stable polarization voltage of 180 mV (inset of Fig. 2a). This shows that the cycle life of the PAM/PVP-coated Zn anodes is 49 times more than that of the bare Zn. The initial large voltage polarization of the PAM/PVP-coated Zn could be ascribed to the instinctive poor conductivities of the non-conductive polymer. The remarkable enhancement of the reversible plating/stripping stability of the Zn anode with the PAM/PVP layer is also observed at a much higher current density of 1.0–5.0 mA cm^{-2} (Fig. S5 and S6†). Fig. 2c shows the rate performance of the cells from 0.2 mA cm^{-2} to 10 mA cm^{-2}, where the PAM/PVP-coated Zn cell exhibits good cycling stability with very regular and minor voltage polarization, whereas the one with bare Zn shows dramatic voltage fluctuations after 18 h of stripping/plating at a small current density of 0.5 mA cm^{-2} (Fig. 2d). In addition, the

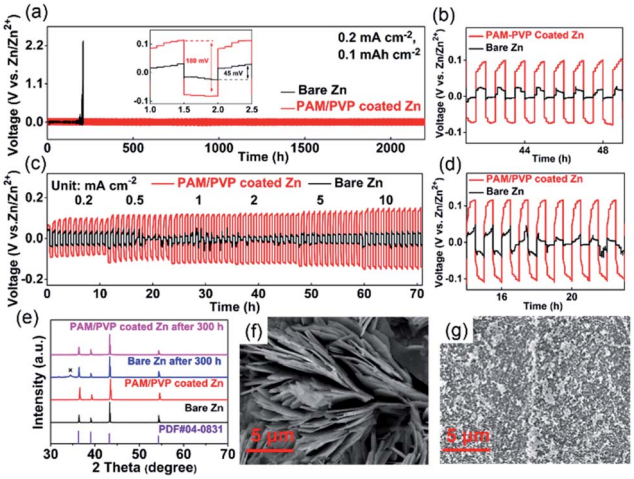

Fig. 2 Electrochemical stability of PAM/PVP-coated Zn anodes. (a) and (c) Voltage profiles of Zn symmetric cells with bare Zn and PAM/PVP-coated Zn at 0.2 mA cm^{-2} and various current densities, respectively. The time of Zn deposition in each cycle is 0.5 h. The inset of a is the detailed voltage profiles of cells. (b) and (d) Magnified view of different cycles in (a) and (c), respectively. (e) XRD patterns of bare Zn and PAM/PVP-coated Zn before and after running for 300 h at a current density of 0.2 mA cm^{-2}. (f) and (g) SEM images of bare Zn and PAM/PVP-coated Zn after cycling for 300 h at a current density of 0.2 mA cm^{-2}, respectively.

current density and capacity increased to 8 mA cm^{-2} & 8 mA h cm^{-2}, and 10 mA cm^{-2} & 10 mA h cm^{-2}, respectively (Fig. S7 and S8†). The voltage curves of the cell with the polymer coating exhibit high electrochemical reversibility with a steady cycling life over 147 h and 80 h, respectively. Meanwhile, an erratic charge/discharge response of the bare Zn can be seen even at the beginning of the profile. The excellent rate performance and good cycling stability further confirm the benefit of the PAM/PVP layer, revealing that this non-conductive polymer-blend layer can offer a steady ion pathway for Zn^{2+} migration and reduce the HER rate. After cycling for 300 h, a new peak at 34.4° of the bare Zn appears in X-ray diffraction (XRD), as shown in Fig. 2e, demonstrating some unknown materials generated on the surface of the bare Zn foil. In contrast, the crystal structure of the Zn anode coated by the PAM/PVP layer is changeless. Fig. 2f and g show the scanning electron microscope (SEM) images of the bare Zn and the PAM/PVP-coated Zn anode after stripping/plating for 300 h. Visible Zn flakes can be seen on the surface of the bare Zn anodes, while a smooth surface without apparent cracks was obtained for the PAM/PVP-coated Zn foil, despite some nanoparticles scattered on top. In an entire plating/stripping process, the Zn^{2+} on the surface of the metal sequentially goes through nucleation, growth and stripping. After nuclei form, an unevenly distributed local electric field is quickly built due to high curvatures, leading to preferential growth of zinc dendrites on the tip area through rapid accumulation of Zn^{2+}. Once the electric field is uniformized, the chance that each site receives Zn^{2+} is well equalized.[43] The reduced accumulation of ions then suppresses the preferential growth of zinc dendrites, giving rise to a smooth

surface even after long-term cycling. Thus, these results somehow reflect the dielectric shielding effect of the non-conductive PAM/PVP thin layer on the local electric field and are consistent with the theoretical simulation of a polymer coating on the uniformization of the local electric field reported previously.[34,35,44–46]

Fig. 3a shows the Tafel curve of the bare Zn and PAM/PVP-coated Zn symmetrical cell in 3 M $Zn(CF_3SO_3)_2$ electrolyte. The corrosion current of the bare Zn anode is decreased from 4.77 mA cm^{-2} to 3.86 mA cm^{-2} after it is coated with a PAM/PVP layer, indicating that the PAM/PVP layer can act as a protection film to decrease the corrosion rate of aqueous electrolytes.[47,48] The mechanism of Zn deposition behavior was tested by chronoamperometry (CA) in Zn symmetric cells (Fig. 3b). The nucleation and surface change of the Zn anode are reflected by the current–time curves.[35,49,50] The current of the bare Zn keeps increasing over 150 s with an overpotential of −200 mV applied, indicating a long and random 2D diffusion process and uncontrolled deposition extension. During plating/stripping, zinc ions would primarily accumulate on the tips in order to minimize the surface energy, thus further accelerating the dendrite growth on the surface of the anode. In comparison, the PAM/PVP-coated Zn anode reaches a stable 3D diffusion after 30 s of planar diffusion and nucleation, suggesting that Zn^{2+} appears to be reduced to Zn^0 with the assistance of 3D controlled diffusion. This result could be attributed to the fact that Zn^{2+} can be transferred to the surface by the functional groups and chains of the PAM and PVP polymers, leading to more nucleation sites that allow the growth of Zn seeds in a smaller size, instead of arbitrary and disordered zinc flakes. The nucleation overpotential and electrochemical reversibility of the bare Zn and the PAM/PVP-coated Zn were investigated at a current density of 1 mA cm^{-2} in a Zn–Ti asymmetric battery. After coating of the PAM/PVP layer, the initial nucleation overpotential increased from −0.1013 to −0.1677 V (Fig. 3c), leading to the formation of more nucleation sites and a smoother deposition layer.[51–53] The coulombic efficiency is an essential criterion to evaluate the life of metallic zinc anodes. The erratic voltage signals and low coulombic efficiency (after plating/stripping for 200 cycles) of the bare Zn–Ti cell are observed (Fig. 3d and f), which is attributed to the side reactions at the interface between the Zn anode and aqueous electrolyte, whereas the PAM/PVP-coated Zn anode shows a regular and smooth voltage profile as well as an average CE of 98.8% from cycle 100 (96.6%) to 300 (98.4%), as shown in Fig. 3e and f. The increase of CE in the initial cycles is mainly attributed to the activation and stabilizing process of the PAM/PVP layer to the electrolyte interface. The lower CE in the initial cycles may also originate from the adsorption and consumption of deposited Zn by the carbon chains and functional groups of PAM/PVP. Furthermore, an improvement in CE with the increase of the plating/stripping rate is detected (Fig. S9†). Such enhanced electrochemical reversibility is attributed to the improved interfacial compatibility and ameliorated transportation channels in Zn^{2+} migration after swelling and cycling of the polymer interphase.

Cyclic voltammetry and galvanostatic charge–discharge were investigated to evaluate the electrochemical window of Zn–AC hybrid ion supercapacitors in 3 M $Zn(CF_3SO_3)_2$ electrolyte with different anodes. Fig. 4a and b show the cyclic voltammetry curves of Zn–AC hybrid ion supercapacitors with different Zn anodes. All of the curves exhibit a quasi-rectangular shape with slightly symmetric humps at both ends. The only difference is that the bare Zn–AC hybrid ion supercapacitors show a steep leap at a voltage over 1.9 V, whereas a relatively weaker leap of the PAM/PVP-coated Zn is observed until a voltage close to 2.1 V. Corresponding to the CV curves, the galvanostatic charge–

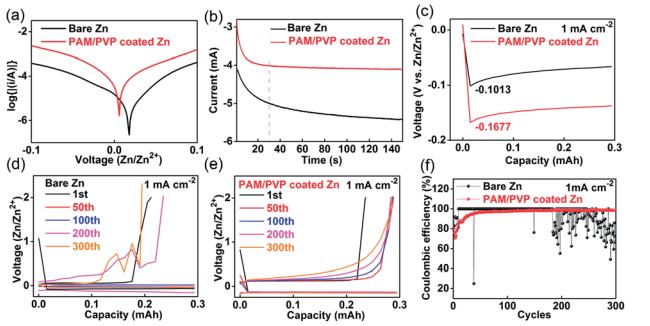

Fig. 3 Nucleation and diffusion mechanism of zinc ions during the plating/stripping process. (a) Tafel curve of the bare Zn and PAM/PVP-coated Zn anode in 3 M $Zn(CF_3SO_3)_2$ electrolyte at a scan rate of 10 mV s^{-1}. (b) Chronoamperograms (CAs) of the bare Zn and PAM/PVP-coated Zn under a −200 mV overpotential. (c) Nucleation energy of the initial Zn plating on Ti foil from the bare Zn and PAM/PVP-coated Zn anodes at 1 mA cm^{-2}. (d) and (e) Voltage profiles of the bare Zn and PAM/PVP-coated Zn in a Zn–Ti cell at a current density of 1 mA cm^{-2}, respectively. (f) Coulombic efficiency (CE) of Zn plating/stripping in the bare Zn–Ti cell and the PAM/PVP-coated Zn–Ti cell at a current density of 1 mA cm^{-2}.

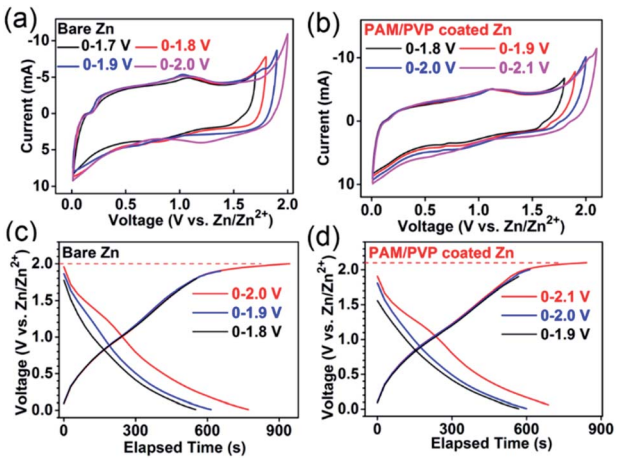

Fig. 4 Electrochemical window of the Zn–AC hybrid supercapacitor in 3 M $Zn(CF_3SO_3)_2$ electrolyte. (a) and (b) Cyclic voltammetry (CV) curves of the Zn–AC hybrid supercapacitor with the bare Zn and PAM/PVP-coated Zn anodes in various voltage ranges at a scan rate of 10 mV s^{-1}, respectively. (c) and (d) Galvanostatic charge–discharge curves of the Zn–AC hybrid supercapacitor with different cutoff voltages at 1 A g^{-1}.

discharge voltage curves of the bare Zn–AC hybrid ion supercapacitors grow asymmetrically when the cutoff voltage exceeds 1.9 V, whereas an overcharge phenomenon can be seen when the voltage reaches 2.0 V (Fig. 4c). For the PAM/PVP-coated Zn–AC hybrid ion supercapacitors, an overcharge curve can be seen until the voltage is beyond 2.1 V (Fig. 4d). These results demonstrate that the optimized electrochemical window of the Zn–AC hybrid ion supercapacitors with bare Zn and PAM/PVP-coated Zn is 1.9 V and 2.0 V, respectively. The oxygen evolution potential increases by 0.1 V with the existence of the PAM/PVP layer, indicating that the PAM/PVP layer can effectively prevent O_2 corrosion in weakly acidic solutions.

The electrochemical performance of the PAM/PVP-coated Zn–AC hybrid ion supercapacitors was tested by cyclic voltammetry and galvanostatic charge–discharge tests within the voltage range of 0–2.0 V (Fig. 5). The CV curves of the hybrid ion capacitors at various scan rates from 10 mV s^{-1} to 200 mV s^{-1} maintain a quasi-rectangular shape, suggesting an EDLC-type behavior (Fig. 5a). Fig. 5b shows the voltage curves of the PAM/PVP-coated Zn–AC hybrid ion supercapacitors at various current densities from 0.5–30 A g^{-1}. The symmetric and linear shape of the curves in the graph

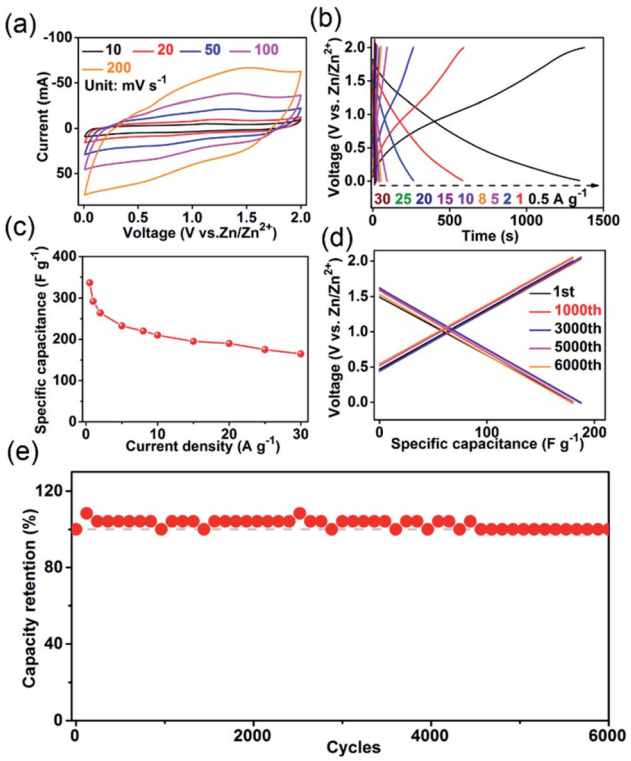

Fig. 5 Electrochemical performance of the PAM/PVP-coated Zn–AC hybrid ion supercapacitors in 3 M $Zn(CF_3SO_3)_2$ electrolyte within a voltage range of 0–2.0 V. (a) Cyclic voltammetry curves of the PAM/PVP-coated Zn–AC hybrid ion supercapacitors at different scan rates from 10 mV s^{-1} to 200 mV s^{-1}. (b) Galvanostatic charge–discharge curves of the PAM/PVP-coated Zn–AC hybrid ion supercapacitors at various current densities (0.5–30 A g^{-1}). (c) Rate capability of the PAM/PVP-coated Zn–AC hybrid ion supercapacitors. (d) and (e) Galvanostatic charge–discharge curves and long-term cycling stability of the PAM/PVP-coated Zn–AC hybrid ion supercapacitors at 15 A g^{-1}, respectively.

can be observed corresponding to the results of the CV test. At a current density of 1 A g^{-1}, the bare Zn–AC hybrid ion supercapacitors failed after 10 cycles, while the PAM/PVP-coated Zn–AC hybrid ion supercapacitors show a good cycling stability (Fig. S10†). This superior stability can be attributed to the critical role of the PAM/PVP layer coated on the zinc anode acting as an inhibitor on the O_2/water interphase and a distributor of ions during the zinc deposition. The PAM/PVP-coated Zn–AC hybrid ion supercapacitors show an excellent rate capability of 336, 292, 264, 232, 220, 195, 190, 175, and 165 F g^{-1} at a current density of 0.5, 1, 2, 5, 8, 10, 15, 20, 25, and 30 A g^{-1} (Fig. 5c and S11†). The galvanostatic charge–discharge curves and long cycling stability of the PAM/PVP-coated Zn–AC hybrid ion supercapacitors at a current density of 15 A g^{-1} are shown in Fig. 5d and e. The specific capacitance of the devices slightly increases at first due to activation, then remains quite stable, and ultimately gives a high retention of 100% of the initial specific capacitance after 6000 cycles. These results further demonstrate the excellent electrochemical performance of the Zn–AC hybrid ion supercapacitors with the PAM/PVP layer. Notably, the PAM/PVP-coated Zn–AC hybrid ion supercapacitors have a high energy density of 118 W h^{-1} kg^{-1} and a power density of 17.9 kW kg^{-1} (based on the mass of AC materials, Fig. S12†), where the energy density is superior to those of the bare Zn–AC hybrid ion supercapacitors (Fig. S13 and Table S1†).[13–17]

Experimental

Materials

Non-ionic polyacrylamide (PAM, $M_w \approx 2\,000\,000$–$14\,000\,000$), polyvinyl pyrrolidone (PVP, $M_w \approx 10\,000$), $Zn(CF_3SO_3)_2$, and polytetrafluoroethylene (PTFE, 60 wt% aqueous dispersion) were all obtained from Shanghai Aladdin Bio-Chem Technology Co., Ltd. Activated carbon YEC-8A (AC) was obtained from Fuzhou Yihuan Carbon Co., Ltd, China. Zn and Ti foils, and Ti mesh were purchased from MTI Co., Ltd. The glass fiber separator was purchased from Whatman Co., Ltd.

Preparation of the PAM/PVP-coated Zn anode

0.01 g of PAM was added to 1.5 mL of deionized water, followed by magnetic stirring for 30 min to give a mixed solution. 0.2 g of PVP was subsequently added under stirring. The mixture was stirred for another 4 h to obtain a solution. This solution was then cast on Zn foil followed by vacuum drying at 110 °C overnight to give the PAM/PVP coating layer (Fig. S14†). The thickness of the polymer layer was measured to be about 14.74 μm, as shown in Fig. S15.† The molar ratio of PAM : PVP, calculated using $[\int(a+d) - 2\int e]/2\int e$ from the integration in ^{1}H NMR (Fig. 1a), is 0.075. Together with the molecular weight of the repeating unit of AM and VP, *i.e.* 71 and 108 g mol^{-1}, respectively, the weight ratio of PAM : PVP in the polymer blend was determined to be 1 : 20.3, which agrees well with the weight ratio in feeding of the two polymers in the preparation (1 : 20).

Material characterization

^{1}H NMR proton spectra in DMSO-d_6 were recorded on a Bruker Avance Spectrometer (500 MHz). TGA and DSC were performed

at a heating and cooling rate of 10 °C min^{-1} using a TA TGA 55 and a TA DSC 25 instrument. XRD measurements were performed by X-ray diffraction (XRD, Bruker D8 Advance diffractometer) with Cu Kα radiation ($\lambda = 1.5405$ Å). The morphology of the Zn anode with and without the polymer coating layer was obtained by scanning electron microscopy (SEM, Zeiss Supra 55). The observation was done directly on the PAM/PVP-coated Zn anode after running without additional surface processing. Dynamic mechanical thermal analysis (DMA) of a free-standing polymer film was performed on an Anton Paar Physica MCR-92 instrument in strain sweep mode from 30 °C to 220 °C. The completely dried PAM and PVP are too brittle for mechanical stretching, and thus a film with controlled wetness was used instead, so as to produce a suitable flexibility for mechanical testing. The humidity and the evaporation speed of the cast process were carefully maintained in a digital drying box to ensure the flexibility of the film specimen. The rheological behavior of the PAM/PVP polymer gel containing $Zn(CF_3SO_3)_2$ was studied with an Anton Paar MCR 302 instrument.

Electrochemical measurements

The Zn symmetric and Zn–Ti asymmetric cells were assembled as CR2030 coin cells to measure the electrochemical performances. Glass fiber and a 3 M $Zn(CF_3SO_3)_2$ aqueous solution were used as the separator and the electrolyte, respectively. Before cell fabrication, Ti foil, bare Zn foil and PAM/PVP-coated Zn were cut into disk-shaped electrodes. The symmetric cells consist of two bare Zn foils (or PAM/PVP-coated Zn foils) separated by a glass fiber separator. The cells underwent galvanostatic charge and discharge cycling at a current density of 0.2–10 mA cm^{-2} on a Neware battery testing instrument. These experiments were performed to evaluate the stripping/plating behavior and cycling stability of the bare Zn and PAM/PVP-coated Zn anodes. Furthermore, Zn–Ti asymmetric cells were fabricated to investigate the coulombic efficiency of Zn stripping/plating. The asymmetric cell was initially discharged for 10 min, and then to 2.0 V at various current densities from 0.2–20 mA cm^{-2}. To obtain the corrosion potential (E_{corr}) and corrosion current density (I_{corr}), Tafel plots of the Zn symmetric cells were recorded on an electrochemical workstation (CHI660E, China) at a scan rate of 10 mV s^{-1}. Chronoamperograms (CAs) of the bare Zn and the PAM/PVP-coated Zn symmetric cells were recorded under a −200 mV overpotential. The Zn–AC hybrid supercapacitors were fabricated with AC as the cathode, bare Zn or PAM/PVP-coated Zn foil as the anode, and 3 M $Zn(CF_3SO_3)_2$ aqueous solution as the electrolyte. The cathode slurry was fabricated by mixing the cathode active materials, Super P, and PTFE at a mass ratio of 80 : 10 : 10. The resulting slurry was rolled into a thin film with a thickness of about 120 μm. Finally, the film was cut into discs with a diameter of 10 mm, pressed into a Ti mesh (15 mm in diameter) and dried in a vacuum oven at 100 °C for 6 h. The electrochemical performance was evaluated by cyclic voltammetry on an electrochemical workstation. The galvanostatic charge–discharge processes of the Zn–AC hybrid supercapacitor were recorded on a Neware battery testing system.

Conclusions

In summary, a simple and cost-effective approach was developed to obtain aqueous Zn–AC hybrid ion supercapacitors with high energy density. This mainly involves using a non-conductive binary polymer blend artificial layer (PAM/PVP) as an artificial interphase on the Zn anode to prevent direct contact of the metal from the aqueous electrolyte. The cooperation of ultra-high molecular weight PAM and low molecular weight PVP ensures strong and stable adhesion of the polymer layer to the surface of the Zn anode. This increased the oxygen evolution potential (0.1 V) and thus inhibited possible corrosion and side reactions from dissolved O_2 and free water. Moreover, the PAM/PVP blend coating uniformizes the localized electric field distribution at the Zn/electrolyte interface, thus avoiding the preferential accumulation of Zn^{2+} on the tip area and suppressing the dendrite growth. Last but not least, the PAM/PVP layer creates a uniform ion flux on the surface of the Zn anode by guiding ion migration along the polar groups, giving rise to a high reversibility for Zn stripping/plating with much smoother Zn deposition and an average coulombic efficiency (CE) of 98.8% at 1 mA cm^{-2}. Consequently, the PAM/PVP-coated Zn–AC hybrid supercapacitor exhibits extraordinary electrochemical performance with a wide operating voltage of 0–2.0 V, high discharge capacitance (336 F g^{-1} at 0.5 A g^{-1}), superior rate performance (≈49.1% capacitance retention at 30 A g^{-1}), high energy/power density (118 W h^{-1} kg^{-1}/17.9 kW kg^{-1} based on the mass of AC materials), and excellent cycling stability with 100% capacitance retention of the initial specific capacitance after 6000 cycles at 15 A g^{-1}. This straightforward and scalable strategy can be easily extended to other systems by rationally selecting a polymer material suitable for different metals and solvents, showing great potential in solving the dendrite issues in advanced metal ion batteries/hybrid capacitors.

Conflicts of interest

The authors declare no conflict of interest.

Acknowledgements

The research was financially supported by Shenzhen Science and Technology Research Grant (China, Grant No. JCYJ20180504165506495). We also gratefully acknowledge support from the National Natural Science Foundation of China (Grant No. 51772240, 21503158, 21905220), and the Key Research and Development Plan of Shaanxi Province (China, Grant No. 2018ZDXM-GY-135).

Notes and references

1 Z. Yang, J. Zhang, M. C. Kintner-Meyer, X. Lu, D. Choi, J. P. Lemmon and J. Liu, *Chem. Rev.*, 2011, **111**, 3577–3613.
2 B. Dunn, H. Kamath and J.-M. Tarascon, *Science*, 2011, **334**, 928–935.
3 D. Larcher and J. M. Tarascon, *Nat. Chem.*, 2015, **7**, 19–29.

4 C. Niu, H. Lee, S. Chen, Q. Li, J. Du, W. Xu, J.-G. Zhang, M. S. Whittingham, J. Xiao and J. Liu, *Nat. Energy*, 2019, **4**, 551–559.
5 J. Xiao, *Science*, 2019, **366**, 426–427.
6 M. Winter and R. J. Brodd, *Chem. Rev.*, 2004, **104**, 4245–4269.
7 Y. Wang, Y. Song and Y. Xia, *Chem. Soc. Rev.*, 2016, **45**, 5925–5950.
8 W. Li, J. R. Dahn and D. S. Wainwright, *Science*, 1994, **264**, 1115–1118.
9 L. Suo, O. Borodin, T. Gao, M. Olguin, J. Ho, X. Fan, C. Luo, C. Wang and K. Xu, *Science*, 2015, **350**, 938–943.
10 C. Xu, B. Li, H. Du and F. Kang, *Angew. Chem., Int. Ed.*, 2012, **51**, 933–935.
11 H. Pan, Y. Shao, P. Yan, Y. Cheng, K. S. Han, Z. Nie, C. Wang, J. Yang, X. Li, P. Bhattacharya, K. T. Mueller and J. Liu, *Nat. Energy*, 2016, **1**, 1–7.
12 D. Kundu, B. D. Adams, V. Duffort, S. H. Vajargah and L. F. Nazar, *Nat. Energy*, 2016, **1**, 1–8.
13 L. Dong, X. Ma, Y. Li, L. Zhao, W. Liu, J. Cheng, C. Xu, B. Li, Q.-H. Yang and F. Kang, *Energy Storage Materials*, 2018, **13**, 96–102.
14 H. Wang, M. Wang and Y. Tang, *Energy Storage Materials*, 2018, **13**, 1–7.
15 S. Wu, Y. Chen, T. Jiao, J. Zhou, J. Cheng, B. Liu, S. Yang, K. Zhang and W. Zhang, *Adv. Energy Mater.*, 2019, 1902915.
16 P. Zhang, Y. Li, G. Wang, F. Wang, S. Yang, F. Zhu, X. Zhuang, O. G. Schmidt and X. Feng, *Adv. Mater.*, 2019, **31**, e1806005.
17 X. Zhang, Z. Pei, C. Wang, Z. Yuan, L. Wei, Y. Pan, A. Mahmood, Q. Shao and Y. Chen, *Small*, 2019, e1903817.
18 T. K. A. Hoang, T. N. L. Doan, K. E. K. Sun and P. Chen, *RSC Adv.*, 2015, **5**, 41677–41691.
19 B. Tang, L. Shan, S. Liang and J. Zhou, *Energy Environ. Sci.*, 2019, **12**, 3288–3304.
20 Z. Liu, Y. Huang, Y. Huang, Q. Yang, X. Li, Z. Huang and C. Zhi, *Chem. Soc. Rev.*, 2019, **49**, 180–232.
21 Y. Tang, C. Liu, H. Zhu, X. Xie, J. Gao, C. Deng, M. Han, S. Liang and J. Zhou, *Energy Storage Materials*, 2020, **27**, 109–116.
22 L. Ma, S. Chen, N. Li, Z. Liu, Z. Tang, J. A. Zapien, S. Chen, J. Fan and C. Zhi, *Adv. Mater.*, 2020, **32**, e1908121.
23 Z. Zhao, F. Li, J. Zhao, G. Ding, J. Wang, X. Du, Q. Zhou, G. Hou and G. Cui, *Adv. Funct. Mater.*, 2020, **30**, 2000347.
24 F. Wang, O. Borodin, T. Gao, X. Fan, W. Sun, F. Han, A. Faraone, J. A. Dura, K. Xu and C. Wang, *Nat. Mater.*, 2018, **17**, 543–549.
25 H. Qu, J. Ju, B. Chen, N. Xue, H. Du, X. Han, J. Zhang, G. Xu, Z. Yu, X. Wang and G. Cui, *J. Mater. Chem. A*, 2018, **6**, 23720–23729.
26 L. Wang, Y. Zhang, H. Hu, H. Y. Shi, Y. Song, D. Guo, X. X. Liu and X. Sun, *ACS Appl. Mater. Interfaces*, 2019, **11**, 42000–42005.
27 N. Zhang, F. Cheng, Y. Liu, Q. Zhao, K. Lei, C. Chen, X. Liu and J. Chen, *J. Am. Chem. Soc.*, 2016, **138**, 12894–12901.
28 J. Zhao, J. Zhang, W. Yang, B. Chen, Z. Zhao, H. Qiu, S. Dong, X. Zhou, G. Cui and L. Chen, *Nano Energy*, 2019, **57**, 625–634.
29 S. Chen, R. Lan, J. Humphreys and S. Tao, *Energy Storage Materials*, 2020, **28**, 205–215.
30 K. Leng, G. Li, J. Guo, X. Zhang, A. Wang, X. Liu and J. Luo, *Adv. Funct. Mater.*, 2020, 2001317.
31 Y. Yamada, J. Wang, S. Ko, E. Watanabe and A. Yamada, *Nat. Energy*, 2019, **4**, 269–280.
32 Q. Zhang, J. Luan, Y. Tang, X. Ji and H. Y. Wang, *Angew. Chem., Int. Ed.*, 2020, **132**, 2–14.
33 J. Zheng, Q. Zhao, T. Tang, J. Yin, C. D. Quilty, G. D. Renderos, X. Liu, Y. Deng, L. Wang, D. C. Bock, C. Jaye, D. Zhang, E. S. Takeuchi, K. J. Takeuchi, A. C. Marschilok and L. A. Archer, *Science*, 2019, **366**, 645–648.
34 L. Kang, M. Cui, F. Jiang, Y. Gao, H. Luo, J. Liu, W. Liang and C. Zhi, *Adv. Energy Mater.*, 2018, **8**, 1801090.
35 Z. Zhao, J. Zhao, Z. Hu, J. Li, J. Li, Y. Zhang, C. Wang and G. Cui, *Energy Environ. Sci.*, 2019, **12**, 1938–1949.
36 H. Yang, Z. Chang, Y. Qiao, H. Deng, X. Mu, P. He and H. Zhou, *Angew. Chem., Int. Ed.*, 2020, **132**, 1–6.
37 R. Yuksel, O. Buyukcakir, W. K. Seong and R. S. Ruoff, *Adv. Energy Mater.*, 2020, 1904215.
38 K. Zhao, C. Wang, Y. Yu, M. Yan, Q. Wei, P. He, Y. Dong, Z. Zhang, X. Wang and L. Mai, *Adv. Mater. Interfaces*, 2018, **5**, 1800848.
39 P. Liang, J. Yi, X. Liu, K. Wu, Z. Wang, J. Cui, Y. Liu, Y. Wang, Y. Xia and J. Zhang, *Adv. Funct. Mater.*, 2020, 1908528.
40 M. d. P. Buera, G. Levi and M. Karel, *Biotechnol. Prog.*, 1992, **8**, 144–148.
41 M. Hadener, I. Gjuroski, J. Furrer and M. Vermathen, *J. Phys. Chem. B*, 2015, **119**, 12117–12128.
42 I. A. Safo, M. Werheid, C. Dosche and M. Oezaslan, *Nanoscale Adv.*, 2019, **1**, 3095–3106.
43 A. Wang, Q. Deng, L. Deng, X. Guan and J. Luo, *Adv. Funct. Mater.*, 2019, **29**, 1902630.
44 X. Kong, P. E. Rudnicki, S. Choudhury, Z. Bao and J. Qin, *Adv. Funct. Mater.*, 2020, **30**, 1910138.
45 C. Deng, X. Xie, J. Han, Y. Tang, J. Gao, C. Liu, X. Shi, J. Zhou and S. Liang, *Adv. Funct. Mater.*, 2020, 2000599.
46 S. B. Wang, Q. Ran, R. Q. Yao, H. Shi, Z. Wen, M. Zhao, X. Y. Lang and Q. Jiang, *Nat. Commun.*, 2020, **11**, 1634.
47 M. Abdallah, *Corros. Sci.*, 2003, **45**, 2705–2716.
48 M. S. Abdel-Aal, Z. A. Ahmed and M. S. Hassan, *J. Appl. Electrochem.*, 1992, **22**, 1104–1109.
49 J. M. Wang, L. Zhang, C. Zhang and J. Q. Zhang, *J. Power Sources*, 2001, **102**, 139–143.
50 C. J. Lan, C. Y. Lee and T. S. Chin, *Electrochim. Acta*, 2007, **52**, 5407–5416.
51 L. E. Morón, A. Méndez, F. Castañeda, J. G. Flores, L. Ortiz-Frade, Y. Meas and G. Trejo, *Surf. Coat. Technol.*, 2011, **205**, 4985–4992.
52 M. Monev, L. Mirkova, I. Krastev, H. Tsvetkova and S. Rashkov, *J. Appl. Electrochem.*, 1998, **28**, 1107–1112.
53 L. Oniciu and L. Muresan, *J. Appl. Electrochem.*, 1991, **21**, 565–574.